The spatial structure of a nonlinear receptive field

Gregory W. Schwartz[1], **Haruhisa Okawa**[1], **Felice A. Dunn**[1], **Josh L. Morgan**[2], **Daniel Kerschensteiner**[3], **Rachel O. Wong**[1], and **Fred Rieke**[1,4]

[1]University of Washington, Seattle, WA

[2]Harvard University, Cambridge, MA

[3]Washington University, St. Louis, MO

[4]Howard Hughes Medical Institute

Abstract

Understanding a sensory system implies the ability to predict responses to a variety of inputs from a common model. In the retina, this includes predicting how the integration of signals across visual space shapes the outputs of retinal ganglion cells. Existing models of this process generalize poorly to predict responses to novel stimuli. This failure arises in part from properties of the ganglion cell response that are not well captured by standard receptive field mapping techniques: nonlinear spatial integration and fine-scale heterogeneities in spatial sampling. Here, we characterize a ganglion cell's spatial receptive field using a mechanistic model based on measurements of the physiological properties and connectivity of only the primary excitatory circuitry of the retina. The resulting simplified circuit model successfully predicts ganglion cell responses to a variety of spatial patterns and thus provides a direct correspondence between circuit connectivity and retinal output.

Introduction

Spatial structure in light inputs is conveyed from the photoreceptors to the inner retina where it is sampled by the dendrites of the retinal ganglion cells (RGCs), the output cells of the retina. Empirical models dominate our quantitative characterization of this spatial integration process. Such models have been refined over the past several decades and in many cases can accurately describe responses to the same stimuli to which the models are fit[1–3]. No models for spatial integration, however, accurately predict the responses of individual RGCs across a wide range of spatial inputs. Further, empirical models by design do not provide a detailed basis for spatial sensitivity in terms of anatomical and physiological features of the retinal circuitry.

Two features of spatial integration in RGCs present major obstacles for a predictive model: nonlinearity and fine-scale heterogeneity. Enroth-Cugell and Robson[4] classified cat retinal ganglion cells based on whether they linearly ("X" cells) or nonlinearly ("Y" cells) integrated inputs across space; RGCs showing nonlinear spatial integration have since been identified in many species[5–8]. Standard approaches to receptive field mapping, such as those based on spike-triggered averaging, fail to capture nonlinear spatial integration. Bipolar cells were initially proposed[9,10] and then demonstrated[11] to be the substrate for nonlinear subunits in the RGC receptive field. A remaining challenge is determining which types of bipolar cell provide input to a given type of RGC and how the sampling of these bipolar cell inputs shapes RGC sensitivity.

Heterogeneity in spatial sampling among individual RGCs of the same type also represents a major obstacle for predictive models. RGC receptive fields exhibit large-scale structure that deviates from either circular or elliptical Gaussian profiles[12]. Heterogeneities on a finer scale have been measured as "hot-spots" within the receptive field that are unique for each RGC[13–16]. Brown et al.[15] measured fine-scale heterogeneity in the receptive fields of rabbit RGCs, but did not find a clear correspondence between the receptive field hot-spots and the dendritic patterns of individual RGCs. They proposed that incorporating information about bipolar cell-to-RGC connectivity might clarify such a correspondence.

A predictive model of RGC spatial integration would have broad implications for understanding retinal circuits. A model based directly on anatomical and physiological mechanisms would by necessity incorporate some aspects of the retinal circuitry and neglect others; a successful model would thus identify aspects of the circuit that are essential to characterize and how they shape spatial sensitivity. Such a model would also help explain how spatial integration changes as the circuitry shaping the responses changes - e.g. as signals shift from the rod bipolar to cone bipolar circuits with increasing light levels. Finally, a successful predictive model would provide a powerful tool with which to explore computationally how populations of RGCs encode the enormous space of visual patterns.

Results

Nonlinear and heterogeneous spatial integration

We studied a distinct functional and morphological cell type in mouse retina that is identified by its large soma, large and sparse dendrites and high contrast sensitivity (anatomically characterized as the G10 RGC[17] and referred to below as the On alpha-like RGC[18,19]). We mapped the linear receptive fields of these cells using standard white noise stimuli (Fig. 1a–c). Consistent with results from other RGC types and other species, the spatial profile of the receptive field center contained hot-spots that were not well fit by a two-dimensional Gaussian profile[13–16] (e.g. one-dimensional receptive field profile in Fig. 1b). Further, and again consistent with other RGCs[5–9], responses to temporally-modulated stimuli showed clear evidence for nonlinear spatial integration (Fig. 1d): spatially uniform stimuli elicited a response dominated by the modulation frequency (top), while temporal modulation of light and dark bars elicited a response at twice the modulation frequency (bottom). Such 'frequency doubling' is a hallmark of nonlinear spatial integration[10]. The frequency-doubled response reached a peak for gratings with a spatial scale ~40 μm and

declined substantially only when the spatial scale exceeded the ~300 μm RGC receptive field center, presumably stimulating the surround (Fig. 1e).

The stimuli and analyses illustrated in Fig. 1 and related studies highlight that RGCs do not integrate space linearly or smoothly. These approaches, however, provide incomplete information about alternative receptive field models since white noise approaches typically assume linear spatial integration[20,21], and grating stimuli characterize sensitivity to spatial scale but not position in two dimensions. Thus we turned to stimuli and analyses that probed heterogeneity and nonlinearity more effectively. In particular, we studied responses to random textures (see Methods for details of stimulus construction).

As expected from the grating responses (Fig. 1d, e), nonlinear spatial integration was apparent in responses to texture stimuli that had structure on a fine spatial scale but little or no structure on the scale of the entire receptive field center (Fig. 2a). Cells responded robustly to these texture patterns with a dependence on spatial scale similar to that observed with grating stimuli (Fig. 2b). Such structure is expected from a receptive field composed of nonlinear subunits, but cannot be explained by a global nonlinearity applied after linear spatial integration (e.g. in standard linear-nonlinear receptive field models)[21].

To probe fine-scale heterogeneity in the spatial sensitivity profiles of individual RGCs, we measured responses to three variants of these texture stimuli: (1) a change in the random seed used to construct the texture (Fig. 2c); (2) small translations of the texture (Fig. 2d); and, (3) rotations of the texture about its center (Fig. 2e). These stimuli should produce little or no response modulation if they are perfectly centered on a receptive field that integrates over space radially symmetrically. This lack of response modulation holds true for receptive fields constructed from linear or nonlinear subunits. On alpha-like RGCs, however, were sensitive to all three manipulations, with unique response profiles for each cell (compare top and bottom response profiles in Fig. 2c–e). Errors in the centering of the stimulus with respect to the RGC dendrites, typically less than 30 μm, could not account for the differences we observed (Supplementary Fig. S1). This sensitivity highlights the need to incorporate fine-scale heterogeneity and nonlinearity into descriptions of RGC receptive fields.

We focused on the rotation condition because it is least influenced by the large-scale Gaussian profile of the receptive field center. Specifically, rotation of a fixed spatial pattern should not modulate the response of any radially symmetric mechanism, independent of whether the mechanism is composed of linear or nonlinear subunits. For a smooth but elongated mechanism, such as an elliptical Gaussian, responses should vary slowly and periodically with rotation angle. Supplemental results show the sensitivity of RGCs to translations of different sizes (Supplementary Fig. S2), to translations of natural patterns (Supplementary Fig. S3), and to texture patterns generated from different random seeds (Supplementary Fig. S4). Our aim below is to identify the anatomical and physiological mechanisms responsible for heterogeneity and nonlinearity in RGC spatial integration and to characterize these mechanisms in sufficient detail that they can be used to construct a quantitative, predictive model for responses like those in Fig. 2.

Excitatory input dominates nonlinear spatial integration—How closely does the receptive field reflect the excitatory synaptic input provided by bipolar cells? To answer this question we compared the excitatory inputs and spike outputs of the same On alpha-like RGC elicited by a rotating texture (Fig. 3). The response patterns were nearly identical (Fig. 3c; $r^2 = 0.97 \pm 0.005$, mean $\pm$ s.e.m, 4 cells).

We also characterized the sensitivity of the ganglion cell responses to rotation angle using linear Fisher information, a measure that defines the error bound of an optimal linear decoder (see Methods). The information contained in the spikes and that contained in the excitatory input were not distinguishable when measured from the same cells (connected points in Fig. 3d). These results indicate that sensitivity to texture rotation is dominated by changes in a RGC's excitatory synaptic input, with little contribution from inhibitory inputs or intrinsic properties (see Discussion). Thus we focused on identifying the bipolar cell type(s) that provide excitatory input to On alpha-like RGCs.

Type 6 bipolar cells provide majority of excitatory input—The unique response profiles of On alpha-like RGCs could be shaped by the sparse pattern of the ganglion cell's dendrites and their connectivity with the bipolar cell mosaics, as suggested previously[15]. To test this proposal, we first determined which bipolar cell types dominate excitatory input to On alpha-like RGCs and then characterized both the properties of the excitatory input these cells provide and their connectivity with the RGC dendrites.

RGCs receive input from a subset of bipolar cell types in part due to the specific stratification patterns of the bipolar cell axon terminals and RGC dendrites[22,23]. Can a single bipolar cell type provide the substrate for nonlinear subunits? To answer this question, we first measured the fraction of the excitatory synapses on the RGC dendrites made by type 6 bipolar cells, which make numerous synaptic contacts with On alpha-like ganglion cells[24].

Synapses between type 6 bipolar cells and On alpha-like RGC dendrites were identified by combining biolistic techniques with transgenic labeling of cells. Retinas were labeled with four distinct markers (Fig. 4a–f): RGCs were biolistically cotransfected with a red fluorescent protein (tdTomato) to visualize their dendrites and a tagged postsynaptic density protein (PSD95-CFP) to label excitatory postsynaptic sites[24]; all On bipolar cells were labeled genetically[25] (*Grm6-YFP*); and type 6 bipolar cells were labeled by Synaptotagmin-2 immunostaining[22] (Syt2). On alpha-like RGCs were identified by their large somas and dendritic morphology. The quadruple label allowed us to determine whether each post-synaptic site on the RGC was opposed to an On bipolar cell (Fig. 4c), and if so, whether that bipolar cell was type 6 (Fig. 4d,e, see Supplementary Movie M1). Putative synapses with type 6 bipolar cells were distributed evenly throughout the dendritic tree of the ganglion cell, and across experiments represented ~70% of the identified inputs from On bipolar cells (Fig. 4f; Supplementary Table S1). Due to the dim and somewhat patchy nature of the Syt2 label, some contacts with type 6 bipolar cells were likely missed in our analysis. This percentage, therefore, represents a lower bound on the proportion of type 6 bipolar cell inputs. An independent measurement of the proportion of type 6 bipolar cell inputs gave a similar result (see Methods).

Type 7 bipolar cells have also been observed to make synaptic contacts with the On alpha-like RGC[25], so we repeated the synapse counting experiments in a transgenic line with most type 7 bipolar cells labeled[23,26] (Fig. 4g–j, Supplementary Movie M2). While particular type 7 bipolar cells often made multiple synaptic contacts with the RGC dendrites, consistent with previous results[24], the majority of type 7 bipolar cells did not make any synapses with the On alpha-like RGC. Across experiments, type 7 bipolar cells accounted for less than 5% of the identified excitatory synaptic sites on the RGC (Supplementary Table S2; see Supplementary Movie M2).

Type 6 bipolar cells constitute nonlinear subunits—The numerical predominance of type 6 bipolar cell inputs to the On alpha-like RGC suggests that they provide the anatomical substrate for nonlinear subunits. To test this suggestion, we (1) quantified the spatial scale of nonlinear interactions in the ganglion cell receptive field, and (2) determined whether these spatial nonlinearities were aligned with the locations of type 6 bipolar cells.

We quantified nonlinear interactions between two locations in space by measuring responses to small spots of light presented either individually or simultaneously. Two spatial locations were determined to interact nonlinearly if the response to the spots presented simultaneously significantly differed from the linear sum of the responses to the spots presented individually; the strength of such nonlinear interactions was quantified with a nonlinearity index that measured the deviation from linearity in units of the standard deviation of the responses (see Methods). Since inputs to the RGC dendrites should be integrated linearly or near linearly under voltage clamp, we attribute nonlinearities in the measured currents to the bipolar cell synaptic output. Nonlinear interactions were most frequently observed for spots presented nearby with the average nonlinearity index falling near zero, indicating a linear interaction, when spots were 50–60 μm apart (Fig. 5e). This spatial scale is similar to the spatial scales characteristic of the frequency-doubled response (Fig. 1e) and of responses to random textures (Fig. 2b).

The above results characterize the spatial extent of the nonlinear subunits but do not test the role of type 6 bipolar cells specifically. Hence we recorded excitatory inputs in response to light stimuli targeted to individual type 6 bipolar cells using a mouse (*Grm6:tdTomato*) in which a subset of On bipolar cells are brightly labeled[27] (Fig. 5a–d; see Methods). If the targeted type 6 bipolar cell indeed constituted a nonlinear subunit, we would expect to see a larger nonlinear interaction between a pair of spots presented within its receptive field than for a pair of spots presented across the boundary of its receptive field (Fig. 5f).

The nonlinearity index was significantly larger for two spots located within a circular region with a radius of 19–25 μm centered on the bipolar cell dendrites than it was for spots located across this boundary ($p < 0.01$ across this range; Fig. 5g,h). The radius accounting for the most significant effect was 22 μm ($p < 0.001$; Fig 5h,i), consistent with both the interaction distance between spots (Fig. 5e) and direct measurements of the bipolar cell receptive field[28] (see Fig. 7b). Experimental uncertainties are likely to obscure, rather than inappropriately create, such a correspondence between bipolar cell location and nonlinear interaction strength. For example, some fraction of the many unlabeled bipolar cells could have receptive fields containing the pair of spots, causing scatter in the measured relationship

between bipolar cell position and nonlinear interaction between spots. Further, uncertainty about spot location on the retina or tilt in the photoreceptor array would blur this relationship. Thus the actual correspondence between spatial nonlinearities and the location of type 6 bipolar cells is likely stronger than that revealed by this experiment.

Predicting the unique spatial fingerprint of a RGC—The relationship between spot location relative to the type 6 bipolar cell and interaction strength in the RGC input currents provides physiological evidence that type 6 bipolar cells contribute to nonlinear spatial integration by the ganglion cell. Other bipolar cell types that make numerically fewer synaptic contacts with the On alpha-like RGCs (Fig. 4) could also contribute. Nonetheless, we constructed a model of the receptive field based on (1) the connectivity of the type 6 bipolar cells with the RGC dendrites, (2) the bipolar cell receptive field, and (3) the nonlinear contrast-response function of the ganglion cell's excitatory synaptic inputs.

We previously counted putative synapses between individual type 6 bipolar cells and On-alpha RGCs[24] using the *Grm6:tdTomato* mouse described above (Fig. 5) and biolistic labeling of the ganglion cell dendrites together with expression of PSD95-CFP (as in Fig. 4). Here, we show that this synaptic count depends linearly on the length of dendrite within the territory of the bipolar cell synaptic terminal (Fig. 6a–c). Next we characterized the distribution of the type 6 bipolar cell axon territory areas (Fig. 6d). Because the synaptic terminals of mouse bipolar cells tile space completely[22], we randomly sampled the distribution of territory areas to construct realistic mosaics of the bipolar cell population (see Methods). Using a 2D projection of the dendritic pattern of an On alpha-like RGC, we assigned a weight to each bipolar cell in the model mosaic according to the linear relationship between number of synapses and dendritic length (Fig. 6c, e).

Two physiological properties of the bipolar cell subunits completed the model (Fig. 7a). First, the receptive field of type 6 bipolar cells was measured from their responses to narrow bars of light (Fig. 7b). The dependence of the integrated current on bar position was well described by a circular Gaussian profile (two standard deviation width of 44 ± 8 μm, mean ± s.e.m; $n = 5$) (Fig. 7b). This is considerably larger than expected from the ~15 μm diameter of the bipolar cell dendrites, but is consistent with the only other measurements of mouse cone bipolar cell receptive fields[28]. The relatively large receptive field likely reflects spread of signals through the gap junctions coupling cone bipolar cells to AII amacrine cells[29,30]. The bipolar cell receptive field size was fixed in the model. Second, we measured the nonlinearity in a ganglion cell's excitatory inputs by stimulating the entire receptive field center with uniform 300 μm discs at several contrasts. These large stimuli should uniformly stimulate the population of bipolar cells providing input to the RGC. The integrated current at each contrast was normalized to the maximum to construct the contrast-response function of the excitatory inputs (Fig. 7c). This function is a measure of the average nonlinear transformation occurring between light stimuli and the RGC excitatory input[11].

The full receptive field model (Fig. 7a) was generated by combining the bipolar cell → RGC connectivity map modeled for each recorded RGC as in Figure 6e with the spatial sampling (Fig. 7b) and nonlinearity characteristics (Fig. 7c) of type 6 bipolar cells. The model was entirely constrained by the measurements described above with the only free parameter

being normalization of the overall response. The only visual stimulus used to construct the model for a particular RGC was a uniform disc used to measure the contrast-response function. Thus spatial structure in the responses predicted by the model emerges from the bipolar receptive field, the anatomical estimate of bipolar cell connectivity based on the RGC dendrites, and parameters of the synaptic contacts made by type 6 bipolar cells. Nonetheless, the model generated accurate predictions of stimuli with two-dimensional spatial structure, e.g. the response profile of a ganglion cell across the 8 different rotation angles of the texture stimulus (Fig. 7d). The model predictions generalized to other spatial stimuli as well (see predictions for random textures in Supplementary Fig. S4).

Significance of the model predictions was evaluated by comparing the measured responses to a null prediction generated using a different random rotating texture as model input (see Methods for details). Across a population of cells, the log-likelihood ratio (base 10) between the model prediction for the appropriate vs. null rotating texture was 85 ($\pm$ 26 s.e.m.; $n = 10$) - i.e. the model prediction was ~10^{85} times more likely than the null model.

The model in Figure 7 is based on anatomical estimates of the weights of bipolar cell inputs to ganglion cells. Bipolar cell weights could also be estimated physiologically by generating a grid of bipolar cell positions, as in Figure 6e, and assigning a weight to each bipolar based on a fine-scale receptive field (e.g. Fig. 1a). Although the bipolar cell weights in such a model are estimated using white noise, the model constructed using these weights differs from a standard linear receptive field because the bipolar cell subunits each provide nonlinear input to the ganglion cell with a nonlinearity measured as above. This physiological approach to estimate bipolar cell weights, however, resulted in substantially poorer predictions than the model based on anatomical weights (by a factor of $10^{6.5}$ for the example cell in Supplementary Fig. S5). This failure could arise from inherent difficulty in characterizing spatial nonlinearities using white noise approaches and/or the hundreds of bipolar weights that need to be estimated. A previous study found that receptive fields measured at high resolution with white noise captured gross features of dendritic morphology (as in Fig. 1a) but did not correlate strongly with fine dendritic structure[15]. It remains possible that bipolar cell weights derived from a higher resolution and lower noise receptive field map or those derived from a different spatial stimulus could improve model performance to match or exceed that of models based on the anatomically-defined weights. The question of how to estimate nonlinear bipolar weights from a physiological measurement is an important area of future research.

Factors contributing to prediction accuracy—What factors determine the accuracy of the model predictions? To answer this question we constructed a set of alternate models (Fig. 8). To explore the role of fine-scale heterogeneity in bipolar cell weights (Fig. 6), we compared predictions of the anatomical-weights model with those of models based on a Gaussian distribution of bipolar weights (Fig. 8a, top row). To explore the role of nonlinear spatial integration, we compared models with linear and nonlinear bipolar cell output functions (Fig. 8a, bottom row).

Gaussian receptive field models are often motivated anatomically assuming a constant density of inputs per unit length of RGC dendrite (e.g. Fig. 6c) and the increasing sparseness

of more distal RGC dendrites[31]. In these models the Gaussian receptive field originates from a decrease in the number of synapses with distance from the soma due to the decreasing dendritic coverage, while the strength of individual synaptic contacts is assumed constant or near-constant across the dendritic tree. The assumptions providing the basis for such Gaussian models have been confirmed by anatomical studies[25,32–34]. Such models do not incorporate fine-scale dendritic structure, but instead assume it is accounted for by the Gaussian falloff in input weights with radial distance. Similar to past models[35], we generated a Gaussian model by assigning each cell in the simulated type-6 bipolar cell mosaic a weight based on its distance from the center-of-mass of the RGC dendrites. Predictions from this model were otherwise computed identically to the anatomical-weights model in Figure 7.

Both the fine-scale heterogeneity and nonlinearity of the anatomical-weights model were critical as models with substitutions in either factor failed to predict the measured response profile. The Gaussian model generated a slowly-varying and periodic dependence on rotation angle due to imperfect alignment of the stimulus on the bipolar weights (red traces and points in Fig. 8b and c). With a perfectly centered stimulus, the Gaussian model predicted no dependence on rotation angle (orange traces and points in Fig. 8b and c). Across a population of 80 rotating texture responses from 10 cells, the anatomical-weights model outperformed the Gaussian bipolar cell weights model (likelihood ratio; see Methods) by a factor of 10^{316} and the centered Gaussian model by a factor of 10^{133} (Fig. 8c). Additional tests of the importance of spatial features of the model are described in Supplemental Discussion.

Nonlinear transfer at the bipolar cell output was also critical to the performance of the model. As expected for a stimulus with matching distributions of light intensity above and below the background level, models with a linear bipolar cell output function averaged zero response across texture patterns (Fig. 8d, e) with predictions too far from the data to define a meaningful likelihood ratio ($> 10^{600}$). Such behavior cannot be 'fixed' by a single global nonlinearity, as in linear-nonlinear (LN) or related models; a global nonlinearity would elevate all responses equally - including the response in the absence of a stimulus altogether[21]. The precise shape of the bipolar cell output nonlinearity was relatively unimportant as a model with a simple rectification in place of the measured nonlinearity performed worse than the model with the measured nonlinearity by only a factor of 12.1 across the population (data not shown).

Discussion

Here we show that responses of individual RGCs to arbitrary spatial patterns can be predicted using the measured properties of the bipolar cell inputs to a RGC – receptive field size, connectivity pattern with the RGC, and output nonlinearity. Predictions of this mechanistically-based model were much more accurate than empirical models for spatial selectivity. Further, the model describes how spatial sensitivity depends on connectivity between bipolar cells and ganglion cells and the physiological properties of the signals RGCs receive from their bipolar cell inputs. The generality and implications of this approach are explored in more detail below.

Model simplifications and their validity

Our anatomically based model captures the response profiles of individual RGCs more closely than previous receptive field models based on linear spatial integration or a Gaussian weighting of nonlinear subunits (Fig. 8). The failure of linear models is expected given the clear nonlinearities in spatial integration exhibited by similar cell types in other species[4,7,8]. The failure of Gaussian models indicates that fine structure in the dendrites cannot be captured by a Gaussian falloff in bipolar weights with distance from the soma.

Our model, nonetheless, makes considerable simplifications. We neglected bipolar cells other than type 6 that make excitatory synapses onto the On alpha-like RGC dendrites[26] (Fig. 4). Type 7 bipolar cells provide less than 5% of the excitatory synapses (Fig. 4), and hence are unlikely to play a major role shaping spatial sensitivity. Type 8 bipolar cells, which also stratify with the dendrites of On alpha-like RGCs, have much larger dendritic fields than either type 6 or 7 (ref. 22), so they would be predicted to be less sensitive to texture patterns with fine spatial structure. Based on the similar spatial selectivity of the excitatory synaptic input and spike responses (Fig. 3), the model also neglects pre and post-synaptic inhibition and active properties of the RGC dendrites.

The success of the model in predicting RGC responses to two-dimensional texture patterns (Figs. 7, 8) indicates that, at least for these stimulus manipulations, the model incorporated (and neglected) an appropriate set of circuit mechanisms. Spatial stimuli of increased complexity, especially those including interactions between space and time, will challenge the predictive power of this simplified model, but may serve to highlight the applicability of the anatomically based approach. With targeted physiological measurements and appropriate anatomical markers, other input circuits could be mapped and layered on top of the primary photoreceptor $\rightarrow$ bipolar cell $\rightarrow$ RGC pathway. Even without mapping the additional circuitry, deviations from the type 6 bipolar cell pathway prediction under various stimulus conditions could be used to isolate the functional role of other circuits such as the excitatory input from other bipolar cell types or inhibition either onto the bipolar cell terminals or onto the RGC dendrites.

Quantitatively relating connectivity and function

We report the first identification of a particular bipolar cell type that provides the basis for nonlinear subunits in the RGC receptive field and the first quantitative prediction of the fine structure of the RGC receptive field from the connectivity between the bipolar cell mosaic and the RGC dendrites. Most previous studies of RGC receptive fields have used linear systems approaches and thus assume linear spatial integration by construction[1] (as in the light blue curve in Supplementary Fig. S5c). Models that capture nonlinear spatial integration have used simplifying assumptions about subunit connectivity like a circular Gaussian profile[35] (as in the red curve in Fig. 8b). While a number of groups have speculated about the connection between the dendritic morphology of individual ganglion cells and their spatial receptive fields[15,31–38], they have not established a quantitative link between the two, or have concluded that fine dendritic structure has only a weak and unimportant role in determining how the RGC samples space[31].

The proliferation of specific labels for bipolar cell types[22] along with a growing set of data on retinal connectivity[39] will enable the next generation of receptive field models to incorporate connectivity data into quantitative descriptions of RGC function. As researchers studying other visual areas or other sensory systems begin to uncover how inputs are mapped across the dendritic arbor of a neuron[40], the general approach of incorporating detailed connectivity data into functional models could provide a valuable framework.

Dendritic morphology influences stimulus selectivity

The sparse dendritic morphology of On alpha-like RGCs leads to fine-scale heterogeneity in bipolar cell weights (Fig. 6, Fig. 8a) and contributes to their differential responses to texture patterns presented at slightly different angles or positions (Fig. 2). Models based on Gaussian weighting of nonlinear subunits will be sensitive to textured stimuli, but not to different texture patterns or small movement of a given texture[10,41]. Indeed, our anatomically-defined model was more sensitive to small (15 μm) translations of natural image stimuli than a Gaussian receptive field model (Supplementary Fig. S3). These considerations suggest that the relative density of the RGC dendrites will be a key determinant of selectivity for different spatial features. Indeed, Brown et al.[15] found receptive field hot spots primarily in wide-field ganglion cells and suggested that these cells might respond to different visual features than narrow-field ganglion cells with more dense dendritic arbors.

Fine-scale receptive field structure is not beneficial for all classes of stimuli, but instead should be viewed as a parameter that influences what types of visual stimuli are best encoded. A heterogeneous receptive field will create a different set of ambiguities in a cell's response than a Gaussian receptive field. For example, a small object crossing through the receptive field would create a temporally-modulated response due to the spatial heterogeneity in synaptic weights; a similar response could be produced by temporal modulation of a spatially-invariant object. However, a heterogeneous receptive field is more sensitive than a Gaussian receptive field to the position of a small object (Supplementary Fig. S6) or a small translation of a natural image (Supplementary Fig. S3). The vast array of RGC morphologies[17,42–45] may offer important clues about their stimulus selectivity[35,46–48]. Our anatomically based model of RGC responses could be integrated into future modeling and experimental work aiming to explore the relationship between dendritic morphology and stimulus selectivity.

Encoding and decoding in a heterogeneous population

We have shown that individual RGCs of the same type respond differently to the same stimulus patterns (Fig. 2c–e) based on their unique dendritic branching patterns. The unique response fingerprint provided by the dendrites, together the extensive dendritic overlap of nearby On alpha-like RGCs[45,49], raises several questions about coding in a heterogeneous population. Are the dendrites of neighboring RGCs of the same type positioned in a way that increases correlation between the cells[50] or does independence at a small spatial scale among overlapping dendritic fields allow for more independent encoding of spatial patterns[16]? Is heterogeneity exploited in the encoding of visual patterns by the RGC population, or is it a source of noise limiting the fidelity of the population code? If RGC

selectivity to stimulus features like texture angle or position does carry useful information, how is the signal decoded in downstream circuits? While new experiments will be needed to answer these questions, a predictive model of RGC responses will provide an important tool for modeling the response of a heterogeneous population.

Methods

Recording

Tissue preparation and RGC recordings were performed as described previously[19] except that the retina was affixed to a glass slide covered in D-Poly-Lysine (BD Biosciences, Bedford, MA). Cell-attached recordings with Ames solution in the recording pipette were used to measure spike responses. For whole-cell voltage clamp recordings in RGCs and type 6 bipolars, the internal solution contained (in mM) 105 CsCH3SO3, 10 TEA-Cl, 20 HEPES, 10 EGTA, 5 Mg-ATP, 0.5 Tris-GTP, 2 QX-314, and 0.2 Alexa 488 or 750 (pH ~7.3 with CsOH, ~280 mOsm). RGCs were adapted to the background light level for at least 10 minutes prior to data collection, and data was collected only from cells which had stable and robust spike responses to 10% contrast steps.

The small spot experiments (Fig. 5), were performed in a mouse with sparse labeling of On bipolar cells[29]. A target type 6 bipolar cell was first identified by axon terminal morphology in the two-photon microscope, and its cell body was identified by following the axon. Stimuli were centered on the cell body. Throughout this procedure, laser power was kept low (< 4 mW at the sample) to minimize light exposure. A whole-cell voltage clamp measurement was made from a nearby On alpha-like RGC, and the cell was filled with a fluorescent dye. After the recording, the region of retina was imaged at higher power (~10 mW) so that bipolar dendrites were visible. If the axon of the target bipolar was apposed to the RGC dendrites in a single image plane (Fig. 5c), the data were included in the analysis. Alignment of spots was based on the center of mass of the bipolar dendrites in the high power image (Fig. 5d).

Type 6 bipolar cells were recorded and filled in flat mount retina and identified by morphology and stratification in the IPL after recordings. We approached the bipolar cells by tearing a hole through the inner limiting membrane and ganglion cell layer ~100 μm lateral from the site of recording and moved the patch pipette diagonally through the IPL to reach the On bipolar cell bodies in the inner nuclear layer.

Visual stimulation

Visual stimuli were displayed on a 800×600 pixel OLED array (eMagin, Bellevue, WA) and projected onto the photoreceptors from below. Pixels were either 1.2 or 1.8 μm on the retina. OLED display intensities were calibrated and linearized in software. Throughout stimulation, the retina was illuminated with a uniform background light, b, causing 500–1500 rhodopsin isomerizations per rod per second. Light intensities, I, in the spatial patterns are described in terms of their contrast defined as

$$\frac{I-b}{b} \times 100\%.$$

Checkerboard stimuli used to measure the linear receptive field (Fig. 1a,b) consisted of random patterns of 18 μm squares at either −100% or 100% contrast covering the entire monitor and updated at a frame rate of either 15 Hz or 30 Hz. Frequency-doubled responses (Fig. 1e,f) were measured using square waves in space (−80% to 80% contrast) at a variety of bar widths, masked by a 600 μm diameter circle centered on the recorded cell. The contrast in each pixel within the mask was modulated sinusoidally at 3.75 Hz for 20 cycles per trial.

Texture stimuli were created by convolving a random binary pixel map with a two-dimensional Gaussian filter. The resulting images were cropped by a 300 μm diameter circular mask and renormalized to contain a uniform distribution of contrasts from −100% to 100%. The mean intensity across the texture equaled that of the surrounding background-only region. The spatial scale of the texture is defined as the 2σ width of the Gaussian filter. Textures were presented for 0.5 s with at least 1.5 seconds between trials. Manipulations of the texture stimuli by changing the rotation angle, center location, or random seed are described in the text.

In the single and paired spot experiments (Fig. 5), spot stimuli were 9 μm in diameter, and presented at 300–2000% contrast for 100 ms. For measurements of the type 6 bipolar cell receptive field (Fig. 7b), rectangular bars 9 μm × 72 μm at 1500% contrast were presented for 0.5 s with 1 sec between trials. Bar position was varied in steps of 9 μm parallel to the short dimension.

Uniform discs to measure the contrast response function in the input currents to the RGC (Fig. 7c) were 300 μm in diameter, centered on the RGC. They were presented for 0.5 s with 1.5 s between trials at contrasts ranging from −100% to 100%.

A test pattern presented on the stimulus monitor was imaged after each recording to aid in the registration between visual stimuli and fluorescence images.

Analysis

The linear space-time receptive field (Fig. 1a–c) was calculated as the reverse correlation of the spike train with the random checkerboard stimulus in 5 ms bins. The spatial and temporal filters were de-convolved by an iterative procedure. First we computed an initial spatial projection of the receptive field by taking the maximum intensity value in time at each pixel. The following steps were iterated (usually twice): 1) a two-dimensional Gaussian was fit to a spatial projection of the receptive field, 2) the temporal filter was estimated as the mean time projection for pixels inside the 2σ boundary of the spatial Gaussian, 3) the spatial projection was recomputed along the estimated temporal filter.

Cycle-averaged responses to temporally-modulated bars excluded the first cycle in each trial. The power spectrum of the average response was computed, and we reported the power

of the frequency doubled "F2" component at 7.5 Hz (Fig. 1e). Responses to texture patterns were quantified as the spike count, for cell-attached recordings, or the charge transfer, for whole-cell recordings, during the 0.5 s presentation of the texture corrected for the baseline in the 0.5 s preceding stimulus presentation. To account for time dependent changes over long recordings, response amplitudes were drift corrected by subtracting a baseline obtained from the preceding and subsequent trials. Drift correction did not substantially alter the reported results.

The linear Fisher information, $\mathscr{I}$, for rotated texture stimuli was as[51]:

$$\mathscr{I} = \nabla R(\theta) C^{-1} \nabla R(\theta)$$

where $R(\theta)$ is the mean response for each rotation angle θ, and C is the covariance of the responses across angles.

To assess nonlinear interactions between spot locations (Fig. 5), we quantified the response to each spot presented individually, R_a and R_{ab}, and the response to the spots presented simultaneously, R_{ab}, as the projection of the current trace on each trial along a template derived from the mean response to the simultaneous presentation. The nonlinearity index, NLI, was computed based on these responses and the number of observations of each, N, as follows.

$$NLI = \frac{\langle R_{ab} \rangle - \langle R_a \rangle - \langle R_b \rangle}{\sqrt{\frac{\sigma_{ab}^2}{N_{ab}} + \frac{\sigma_a^2}{N_a} + \frac{\sigma_b^2}{N_b}}}$$

Quantifying the spot responses by the integrated current gave similar results.

Type 6 bipolar cell responses (Fig. 7b) were quantified by the integrated current during presentation of each bar stimulus. Receptive fields were fit in each dimension by a one-dimensional Gaussian. Circularity of the receptive field was assessed in the two cells for which the receptive field was measured in two directions. In these cells, the mean difference between width in the two dimensions was 33%.

Contrast response functions for a RGC's excitatory input (Fig. 7c) were quantified by the integrated current during the presentation of discs at varying contrasts.

To compare the RGC responses to different rotation angles of a texture, $D(\theta)$ to the model output, $M(\theta)$, we first scaled both the data and model to a mean response of unity (Fig. 7; model construction described below). The likelihood of a given model response given the data, ℓ, was calculated as follows:

$$\ell = \prod_\theta P_g \left(\frac{M(\theta) - \langle D(\theta) \rangle}{\sigma_D(\theta)} \right)$$

where P_g denotes the Gaussian probability density function. The likelihood of the model when presented with the same stimulus as the cell, ℓ_{ver}, was compared to null prediction, ℓ_{null}, obtained by presenting the model with a texture stimulus with the same statistics as the real stimulus, but a different random seed. We report log likelihood ratios for the comparison of the veridical to null models averaged over 10 null models with different random seeds, $\langle \log_{10} \frac{\ell_{ver}}{\ell_{null}} \rangle$.

Cell transfection

RGCs were biolistically transfected as described previously[24,25,27]. Briefly, isolated retinas were mounted on nitrocellulose membrane filters RGC side up. Gold particles of 1.6 μm diameter were coated with plasmids encoding CFP-tagged PSD95 or tdTomato under the control of the CMV promoter, and delivered to RGCs using a Helios gene gun (Bio-Rad, Hercules, CA). The retina was then incubated for 24 hrs in mouse artificial cerebral spinal fluid (in mM 119 NaCl, 2.5 KCl, 1.3 MgCl2, 2.5 CaCl2, 1 NaHPO4, 11 glucose, 20 HEPES, pH 7.4) in an oxygenated chamber heated at 33° C. At the end of the incubation, the retina was fixed in 4% (w/v) paraformaldehyde for 20 min, and washed in 0.1 M phosphate buffer saline (PBS, pH 7.4).

Immunohistochemistry

Fixed retinas were cryoprotected in PBS with a sucrose gradient (10%, 20% and 30% w/v), and frozen and thawed twice. The tissue was then incubated in PBS containing mouse monoclonal anti-synaptotagmin 2 (anti-Syt2) antibody (1:200, Zebrafish International Resource Center, University of Oregon, Eugene, OR), 5% normal donkey serum, 0.5% Triton X-100 and 0.05% sodium azide, for 5 days at 4° C. After washing the primary antibody, the tissue was incubated with a donkey anti-mouse IgG DyLight 649 secondary antibody (Jackson ImmunoResearch Laboratories, West Grove, PA) overnight at 4° C.

Imaging

Images of fixed retinas described in Fig. 4 and Fig. 6 were acquired with Olympus FV1000 confocal microscope using 1.35 NA 60x or 1.4 NA 60x oil objectives. The voxel size was $0.103 \times 0.103 \times 0.3$ μm for Fig. 4, and $0.069 \times 0.069 \times 0.2$ μm for Fig. 6. Live images of RGC dendrites along with bipolar cells (Fig. 4) were acquired with a Nikon FN-1 two-photon microscope with 980 nm excitation light using a 1.0 NA 60x objective with a voxel size of $0.414 \times 0.414 \times 0.350$ μm. Images of RGC dendrites for the predictive model (Fig. 6) were acquired either with two-photon illumination at 980 nm using a 0.5 NA 20x objective with a voxel size of $1.24 \times 1.24 \times 1.00$ μm or with one-photon infrared illumination using a 0.25 NA 10x objective with a voxel size of $1.55 \times 1.55 \times 1.50$ μm.

Image analysis

Acquired images were median filtered to remove photomultiplier noise. For the image analysis in Fig. 4, all PSD95 puncta in the entire image were identified as described previously[25] using our custom-written program in Matlab. As shown in Supplemental movies (M1 and M2), each identified PSD95 punctum was visually assessed in 3-D for potential apposition with the axonal terminals of type 6 and type 7 bipolar cells[24]. Type 7

bipolar cell axons were visualized using *Gus-GFP* transgenic mice[22,26]. Type 6 bipolar cell axons were identified by Syt2 immunoreactivity. The intensity of the Syt2 signal was variable across cells, making it more difficult to judge whether a particular type 6 axon was apposed to the G10 dendrite when the immunolabeling was dim. To circumvent this limitation, we used the *Grm6-YFP* transgenic mouse line in which all ON bipolar cell axons are brightly labeled by expression of YFP[25]. In this line, even dimly expressing Syt2 axons could be visualized using the YFP signal (see Supplementary movie M1).

For the image analysis in Fig. 6, pairs of type 6 bipolar cells and On alpha-like RGCs obtained in a previous study[24] were re-analyzed. We arrived at an independent estimate of the proportion of type 6 bipolar contacts from this analysis. We found that a given G10 RGC has on average 0.5 synapses per μm dendrite, so the 0.39 synapses per μm dendrite within the type 6 bipolar cell axonal field (Fig. 6c) represent 78% of the synapses assuming complete tiling of type 6 bipolar cell axon terminals.

Binary masks of bipolar axons and RGC dendrites were created using Amira (Visage Imaging, Berlin, Germany), and projected onto a single z plane to generate polygonal territories of bipolar axon terminals and for skeletonizing RGC dendrites. Numbers of synapses between individual pairs of type 6 bipolar cells and On alpha-like RGCs were obtained from a previous study[24].

Bipolar weights model

Model bipolar cell locations were generated as a jittered hexagonal grid. Grid spacing was 16 μm plus gaussian noise ($\sigma = 2$ μm), and bipolar axon territories were generated by the Voronoi tessellation of these center positions. Randomization of the bipolar positions was varied as described in the text and legends, but other parameters remained fixed. These parameters were chosen so that the distribution of axon territory areas matched both the mean and standard deviation of the measured distribution for type 6 bipolar cells (Fig. 6d).

Images of RGC dendrites were traced by hand. The length of dendrite within the axonal territory of each model bipolar was computed, and the bipolar weight was assigned according to the measured density of 0.39 synapses per μm of dendrite (Fig. 6c). Bipolar weights were rounded to the nearest integer, and each bipolar with a nonzero weight was assigned a circular Gaussian receptive field with a 2σ width of 44 μm normalized to integrate to unity.

Construction of anatomical-weights model

A two dimensional stimulus was represented in the model by the contrast in each pixel, $S(x, y)$. The stimulus was scaled and aligned to match the image of the RGC dendrites. The receptive field of each model bipolar, $F_b(x, y)$, was multiplied point by point with the stimulus and summed. For each bipolar, the resulting contrast value

$$c_b = \sum_{x,y} S(x, y) F_b(x, y)$$

served as the input to the contrast response function, $N(c_b)$ measured for the RGC (Fig. 6c) and linearly interpolated between the measured points. The resulting bipolar responses were each scaled by the bipolar weight, W_b, as described above and summed to give the final model RGC response, M:

$$M = \sum_{b=1}^{N_{bipolars}} W_b N(c_b)$$

To account for the unknown angle of shear between the photoreceptors on which stimuli were presented and the imaged RGC dendrites, we allowed the model to vary the assumed stimulus position by up to 25 μm from the position determined by alignment. We chose the stimulus position that maximized the log likelihood estimate of the model prediction given the measured data. Evidence that this small displacement fitting procedure did not over-fit noise and bias our interpretation of the quality of model fits is given in Supplementary figure S1.

Alternate models

We tested alternate models by systematically substituting pieces of the nonlinear anatomical-weights model described above with more traditional assumptions about spatial integration (Fig. 8 and Supplementary Fig. S5). These substitutions are described below.

Gaussian bipolar weights—Bipolar weights were derived from a two-dimensional Gaussian distribution centered on the center of mass of the RGC dendrites, with a 2σ width matching the largest distance between dendrites. Each bipolar cell was assigned a weight by the distance between the bipolar center and the center of mass of the RGC dendrites. The weight matrix was normalized so that the sum of bipolar weights matched that of the anatomical-weights model. In the optimized Gaussian model, the fit likelihood was optimized by shifting the stimulus arbitrarily relative to the Gaussian weight profile. Supplementary Table S3 summarizes the differences between the anatomical and Gaussian bipolar weights models.

Receptive field measurement weights model—Each bipolar cell received a weight equal to that of the nearest pixel in a spatial receptive field measured as described above with 18 μm flickering squares.

Linear—The contrast response function used as an input-output relationship for each bipolar was replaced by a line of unity slope.

Supplementary Material

Refer to Web version on PubMed Central for supplementary material.

Acknowledgments

References

1. Chichilnisky EJ. A simple white noise analysis of neuronal light responses. Network. 2001; 12:199–213. [PubMed: 11405422]

2. Pillow JW, et al. Spatio-temporal correlations and visual signalling in a complete neuronal population. Nature. 2008; 454:995–999. [PubMed: 18650810]

3. Pillow JW, Paninski L, Uzzell VJ, Simoncelli EP, Chichilnisky EJ. Prediction and decoding of retinal ganglion cell responses with a probabilistic spiking model. J Neurosci. 2005; 25:11003–11013. [PubMed: 16306413]

4. Enroth-Cugell C, Robson JG. The contrast sensitivity of retinal ganglion cells of the cat. J Physiol. 1966; 187:517–552. [PubMed: 16783910]

5. Caldwell JH, Daw NW. New properties of rabbit retinal ganglion cells. J Physiol. 1978; 276:257–276. [PubMed: 650447]

6. Stone C, Pinto LH. Response properties of ganglion cells in the isolated mouse retina. Vis Neurosci. 1993; 10:31–39. [PubMed: 8424927]

7. Petrusca D, et al. Identification and characterization of a Y-like primate retinal ganglion cell type. J Neurosci. 2007; 27:11019–11027. [PubMed: 17928443]

8. Demb JB, Haarsma L, Freed MA, Sterling P. Functional circuitry of the retinal ganglion cell's nonlinear receptive field. J Neurosci. 1999; 19:9756–9767. [PubMed: 10559385]

9. Hochstein S, Shapley RM. Linear and nonlinear spatial subunits in Y cat retinal ganglion cells. J Physiol. 1976; 262:265–284. [PubMed: 994040]

10. Victor JD, Shapley RM. The nonlinear pathway of Y ganglion cells in the cat retina. J Gen Physiol. 1979; 74:671–689. [PubMed: 231636]

11. Demb JB, Zaghloul K, Haarsma L, Sterling P. Bipolar cells contribute to nonlinear spatial summation in the brisk-transient (Y) ganglion cell in mammalian retina. J Neurosci. 2001; 21:7447–7454. [PubMed: 11567034]

12. Gauthier JL, et al. Receptive fields in primate retina are coordinated to sample visual space more uniformly. PLoS Biol. 2009; 7:e1000063. [PubMed: 19355787]

13. Thibos LN, Levick WR. Bimodal receptive fields of cat retinal ganglion cells. Vision Res. 1983; 23:1561–1572. [PubMed: 6666058]

14. Passaglia CL, Troy JB, Ruttiger L, Lee BB. Orientation sensitivity of ganglion cells in primate retina. Vision Res. 2002; 42:683–694. [PubMed: 11888534]

15. Brown SP, He S, Masland RH. Receptive field microstructure and dendritic geometry of retinal ganglion cells. Neuron. 2000; 27:371–383. [PubMed: 10985356]

16. Soo FS, Schwartz GW, Sadeghi K, Berry MJn. Fine spatial information represented in a population of retinal ganglion cells. J Neurosci. 2011; 31:2145–2155. [PubMed: 21307251]

17. Volgyi B, Chheda S, Bloomfield SA. Tracer coupling patterns of the ganglion cell subtypes in the mouse retina. J Comp Neurol. 2009; 512:664–687. [PubMed: 19051243]

18. Pang JJ, Gao F, Wu SM. Light-evoked excitatory and inhibitory synaptic inputs to ON and OFF alpha ganglion cells in the mouse retina. J Neurosci. 2003; 23:6063–6073. [PubMed: 12853425]

19. Murphy GJ, Rieke F. Network variability limits stimulus-evoked spike timing precision in retinal ganglion cells. Neuron. 2006; 52:511–524. [PubMed: 17088216]

20. Gollisch T, Meister M. Eye smarter than scientists believed: neural computations in circuits of the retina. Neuron. 2010; 65:150–164. [PubMed: 20152123]

21. Schwartz GW, Rieke F. Nonlinear spatial encoding by retinal ganglion cells: when 1 + 1   2. Journal of General Physiology. 2011; 138:283–290. [PubMed: 21875977]

22. Wassle H, Puller C, Muller F, Haverkamp S. Cone contacts, mosaics, and territories of bipolar cells in the mouse retina. J Neurosci. 2009; 29:106–117. [PubMed: 19129389]

23. Yamagata M, Sanes JR. Dscam and Sidekick proteins direct lamina-specific synaptic connections in vertebrate retina. Nature. 2008; 451:465–469. [PubMed: 18216854]

24. Morgan JL, Soto F, Wong RO, Kerschensteiner D. Development of cell type-specific connectivity patterns of converging excitatory axons in the retina. Neuron. 2011; 71:1014–1021. [PubMed: 21943599]

25. Morgan JL, Schubert T, Wong RO. Developmental patterning of glutamatergic synapses onto retinal ganglion cells. Neural Dev. 2008; 3:8. [PubMed: 18366789]

26. Lin B, Masland RH. Synaptic contacts between an identified type of ON cone bipolar cell and ganglion cells in the mouse retina. Eur J Neurosci. 2005; 21:1257–1270. [PubMed: 15813935]

27. Kerschensteiner D, Morgan JL, Parker ED, Lewis RM, Wong RO. Neurotransmission selectively regulates synapse formation in parallel circuits in vivo. Nature. 2009; 460:1016–1020. [PubMed: 19693082]

28. Berntson A, Taylor WR. Response characteristics and receptive field widths of on-bipolar cells in the mouse retina. J Physiol. 2000; 524(Pt 3):879–889. [PubMed: 10790165]

29. Dacey D, et al. Center surround receptive field structure of cone bipolar cells in primate retina. Vision Res. 2000; 40:1801–1811. [PubMed: 10837827]

30. Mills SL, Massey SC. Differential properties of two gap junctional pathways made by AII amacrine cells. Nature. 1995; 377:734–737. [PubMed: 7477263]

31. Freed MA, Smith RG, Sterling P. Computational model of the on-alpha ganglion cell receptive field based on bipolar cell circuitry. Proc Natl Acad Sci U S A. 1992; 89:236–240. [PubMed: 1309606]

32. Cohen E, Sterling P. Microcircuitry related to the receptive field center of the on-beta ganglion cell. J Neurophysiol. 1991; 65:352–359. [PubMed: 2016645]

33. Jakobs TC, Koizumi A, Masland RH. The spatial distribution of glutamatergic inputs to dendrites of retinal ganglion cells. J Comp Neurol. 2008; 510:221–236. [PubMed: 18623177]

34. Koizumi A, Jakobs TC, Masland RH. Regular mosaic of synaptic contacts among three retinal neurons. J Comp Neurol. 2011; 519:341–357. [PubMed: 21165978]

35. Zeck GM, Xiao Q, Masland RH. The spatial filtering properties of local edge detectors and brisk-sustained retinal ganglion cells. Eur J Neurosci. 2005; 22:2016–2026. [PubMed: 16262640]

36. Creutzfeldt OD, Sakmann B, Scheich H, Korn A. Sensitivity distribution and spatial summation within receptive-field center of retinal on-center ganglion cells and transfer function of the retina. J Neurophysiol. 1970; 33:654–671. [PubMed: 4318174]

37. Kier CK, Buchsbaum G, Sterling P. How retinal microcircuits scale for ganglion cells of different size. J Neurosci. 1995; 15:7673–7683. [PubMed: 7472518]

38. Koch C, Poggio T, Torre V. Retinal ganglion cells: a functional interpretation of dendritic morphology. Philos Trans R Soc Lond B Biol Sci. 1982; 298:227–263. [PubMed: 6127730]

39. Bock DD, et al. Network anatomy and in vivo physiology of visual cortical neurons. Nature. 2011; 471:177–182. [PubMed: 21390124]

40. Helmstaedter M, Briggman KL, Denk W. High-accuracy neurite reconstruction for high-throughput neuroanatomy. Nat Neurosci. 2011; 14:1081–1088. [PubMed: 21743472]

41. Hochstein S, Shapley RM. Quantitative analysis of retinal ganglion cell classifications. J Physiol. 1976; 262:237–264. [PubMed: 994039]

42. Badea TC, Nathans J. Quantitative analysis of neuronal morphologies in the mouse retina visualized by using a genetically directed reporter. J Comp Neurol. 2004; 480:331–351. [PubMed: 15558785]

43. Sun W, Li N, He S. Large-scale morphological survey of mouse retinal ganglion cells. J Comp Neurol. 2002; 451:115–126. [PubMed: 12209831]

44. Kong JH, Fish DR, Rockhill RL, Masland RH. Diversity of ganglion cells in the mouse retina: unsupervised morphological classification and its limits. J Comp Neurol. 2005; 489:293–310. [PubMed: 16025455]

45. Coombs J, van der List D, Wang GY, Chalupa LM. Morphological properties of mouse retinal ganglion cells. Neuroscience. 2006; 140:123–136. [PubMed: 16626866]

46. Masland RH. The fundamental plan of the retina. Nat Neurosci. 2001; 4:877–886. [PubMed: 11528418]

47. Amthor FR, Takahashi ES, Oyster CW. Morphologies of rabbit retinal ganglion cells with complex receptive fields. J Comp Neurol. 1989; 280:97–121. [PubMed: 2918098]

48. Kim IJ, Zhang Y, Yamagata M, Meister M, Sanes JR. Molecular identification of a retinal cell type that responds to upward motion. Nature. 2008; 452:478–482. [PubMed: 18368118]

49. Wassle H, Peichl L, Boycott BB. Dendritic territories of cat retinal ganglion cells. Nature. 1981; 292:344–345. [PubMed: 7254331]

50. Ala-Laurila P, Greschner M, Chichilnisky EJ, Rieke F. Cone photoreceptor contributions to noise and correlations in the retinal output. Nat Neurosci. 2011; 14:1309–1316. [PubMed: 21926983]

51. Abbott LF, Dayan P. The effect of correlated variability on the accuracy of a population code. Neural Comput. 1999; 11:91–101. [PubMed: 9950724]
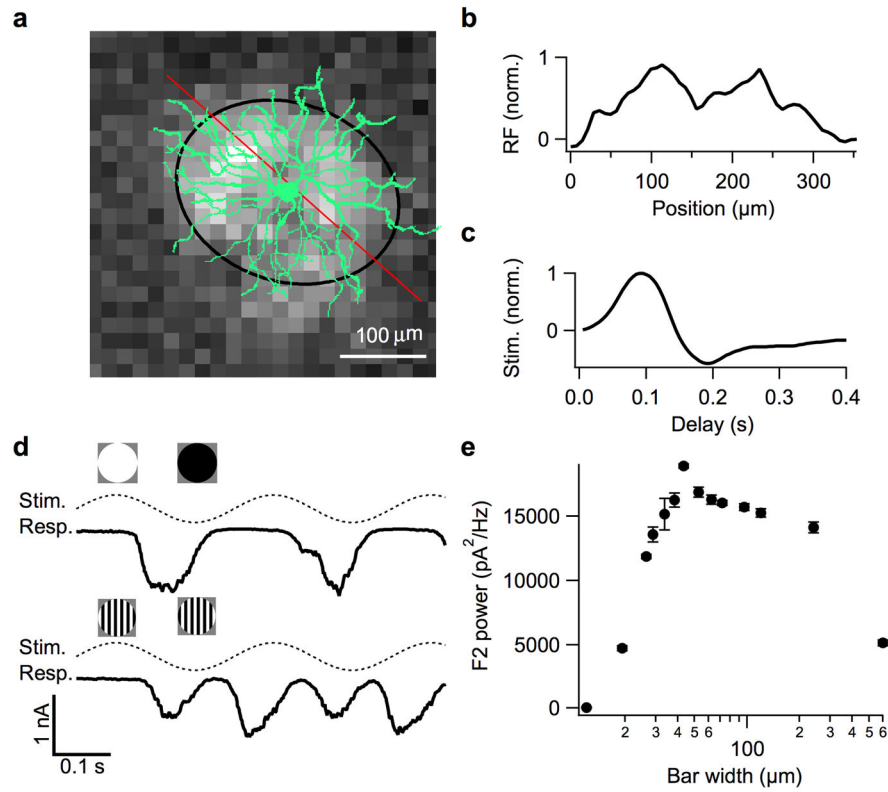
Figure 1. The receptive fields of On alpha-like RGCs have heterogeneous structure and nonlinear subunits

a, Image of a RGC superimposed on the spatial component of the linear receptive field derived from white noise stimulation. Ellipse is the 2σ Gaussian profile. **b**, One-dimensional profile of a slice of the receptive field denoted by the red line in **a. c**, Average temporal filter from the pixels inside the ellipse in **a. c**, Excitatory input currents elicited by temporally-modulated discs (*top*) and 44 µm bars (*bottom*; see Methods). **d**, Frequency doubled response power as a function of bar width.
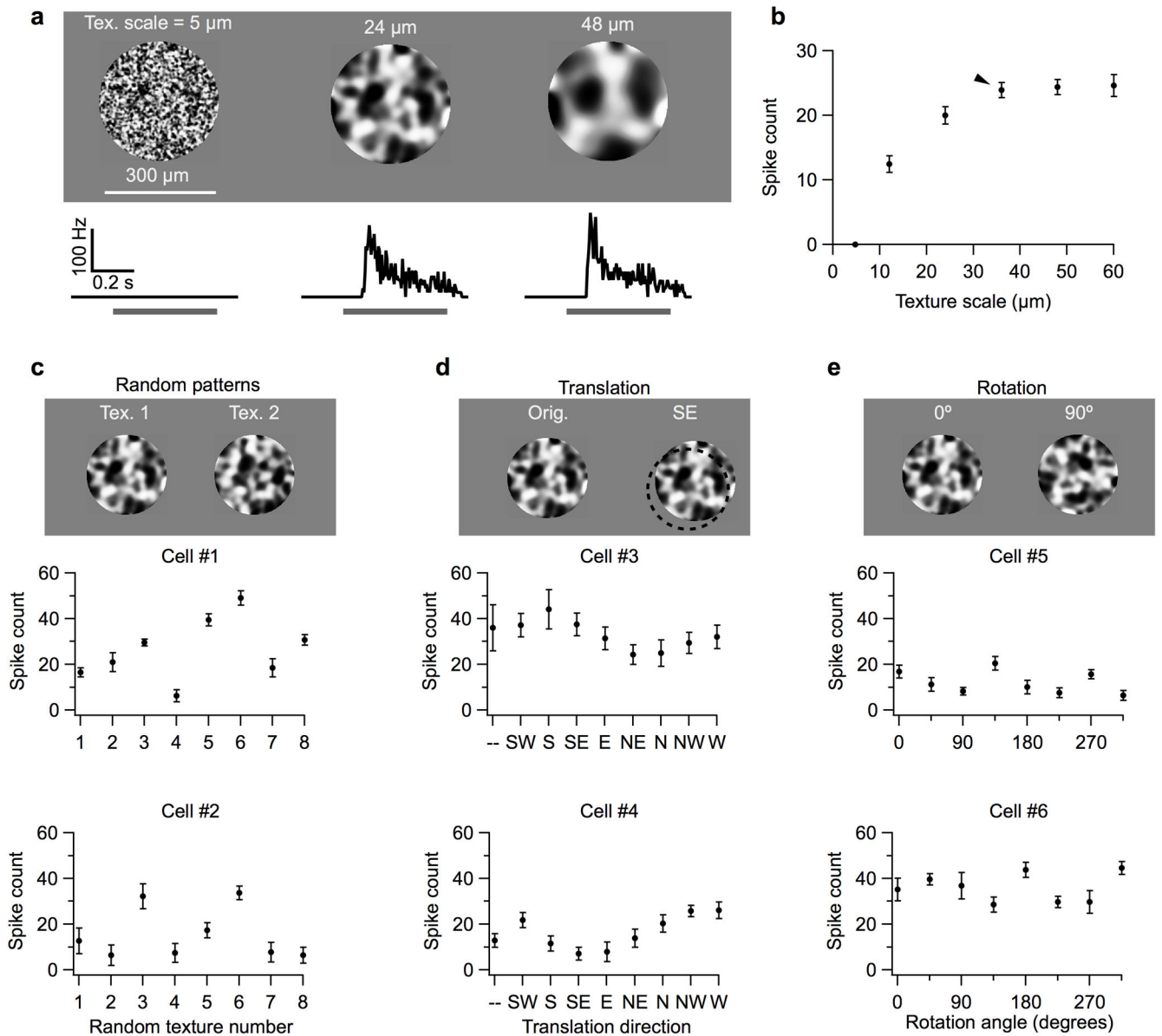
Figure 2. Nonlinear and heterogeneous receptive field properties cause unique responses to stimuli with fine spatial structure

a, *Top*, Texture stimuli with different spatial scales (see Methods for stimulus construction). *Bottom,* firing rate of an example cell in response to the presentation of each texture stimulus shown above. Textures were flashed for 0.5 s with 1 s blank between trials with a maintained light level throughout. Gray bar indicates texture presentation. **b**, Mean spike count as a function of the spatial scale of the texture. Error bars are s.e.m. across cells (*n* = 7). Arrowhead indicates spatial scale used for the stimuli in panels **c–e. c**, *Top*, Examples of two texture stimuli generated with different random seeds. *Middle and bottom,* responses of two different On alpha-like RGCs to texture stimuli generated with eight random seeds. **d**, Stimulus examples and responses elicited by the same texture stimulus translated 33 µm in

eight different directions. **e,** Stimulus examples and responses elicited by the same texture stimulus presented at eight different rotation angles. Error bars in **c–e** are s.d. across trials.
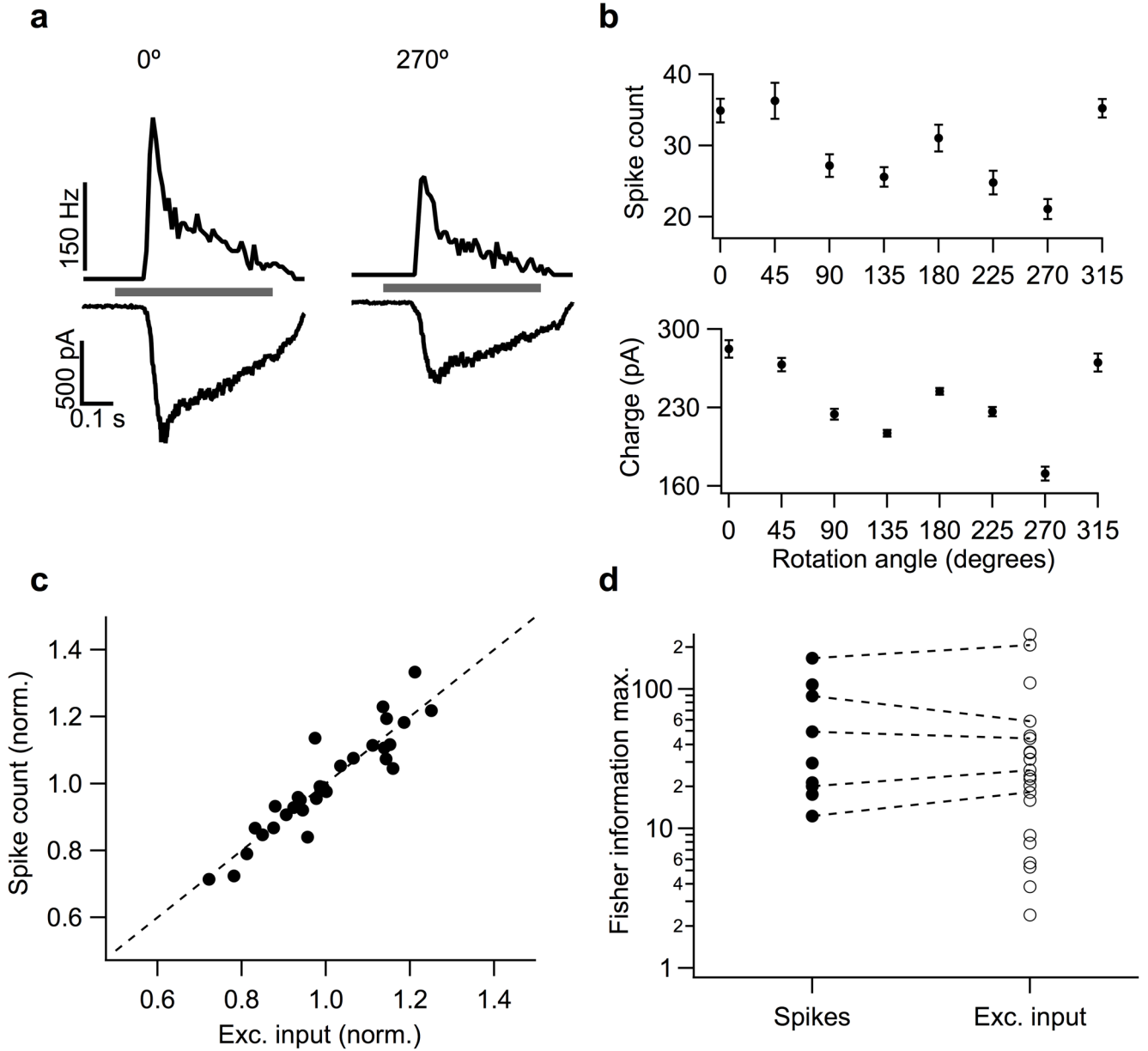
Figure 3. Excitatory inputs and spike response share similar sensitivity to rotation
a, Average firing rate and excitatory input current measured from the same cell in response to a texture stimulus presented at two different rotation angles. Gray bar indicates texture presentation. **b**, Spike count (*top*) and charge transfer in excitatory input currents (*bottom*) at each rotation angle for the cell in **a. c**, Normalized spike count vs. normalized change transfer of excitatory input current in response to rotations of a texture stimulus (*n* = 4 cells 32 total angles). Dashed line is unity. **d**, Maximum linear Fisher information about rotation angle across different texture scales for spike counts or charge transfer (see Methods). Dashed lines connect points from the same cell.
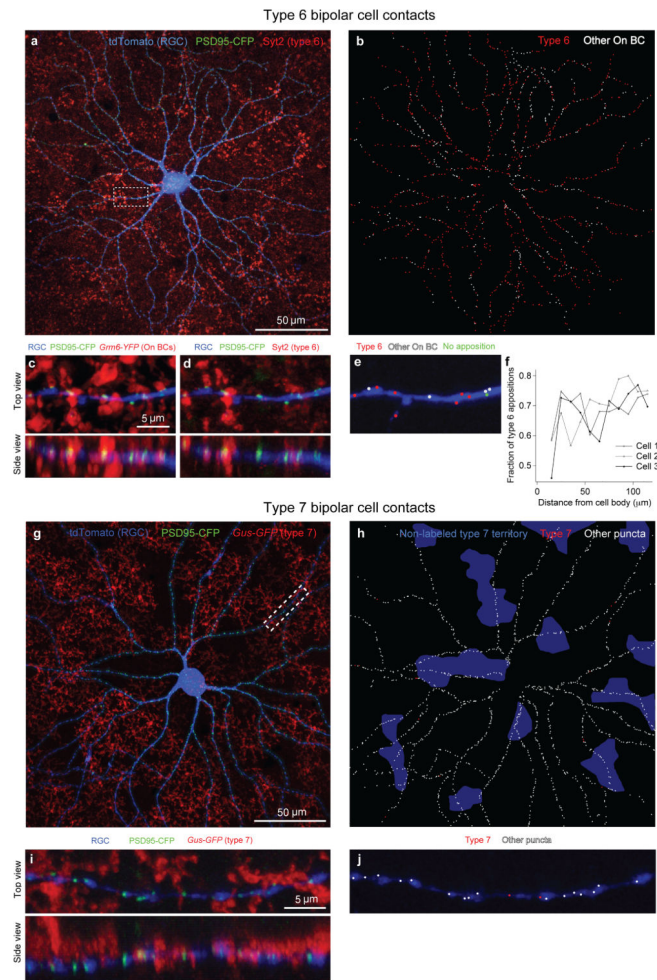
Figure 4. Type 6 bipolar cells contact the majority of excitatory post-synaptic sites on the On alpha-like RGC

a, On alpha-like RGC filled with tdTomato (blue) with labelled putative post-synaptic sites identified by puncta of postsynaptic density protein PSD95-CFP (green). Type 6 bipolar cell axon terminals are labelled with an antibody to Synaptotagmin-2 (Syt2, red). All On bipolar cells were labelled by *Grm6-YFP* (not shown in this panel). Boxed region is inset for **c–e. b**, Putative post-synaptic sites from **a** are colored according to whether they were apposed to a type 6 bipolar cell (red) or a different On bipolar cell (white). **c**. Top and side views of a stretch of the RGC dendrite. All On bipolar cells are labelled by *Grm6-YFP* (red). **d**. Same region as in **c** with only the type 6 bipolar cell label (Syt2) shown in red. **e**. Synapse identification for the region in **c,d. f**, Fraction of type 6 bipolar cell synaptic contacts as a function of distance from the soma for 3 cells. **g.** A different On alpha-like RGC labelled as in **a**, in a genetic background with type 7 bipolar cells labelled (*Gus-GFP*; red). Boxed region is inset for **i,j. h**. Identification of type 7 synaptic contacts. Blue shows regions lacking type 7 cone bipolar labeling. **i**. Magnified view of a stretch of RGC dendrite. **j**. Synapse identification for the region in **i**.
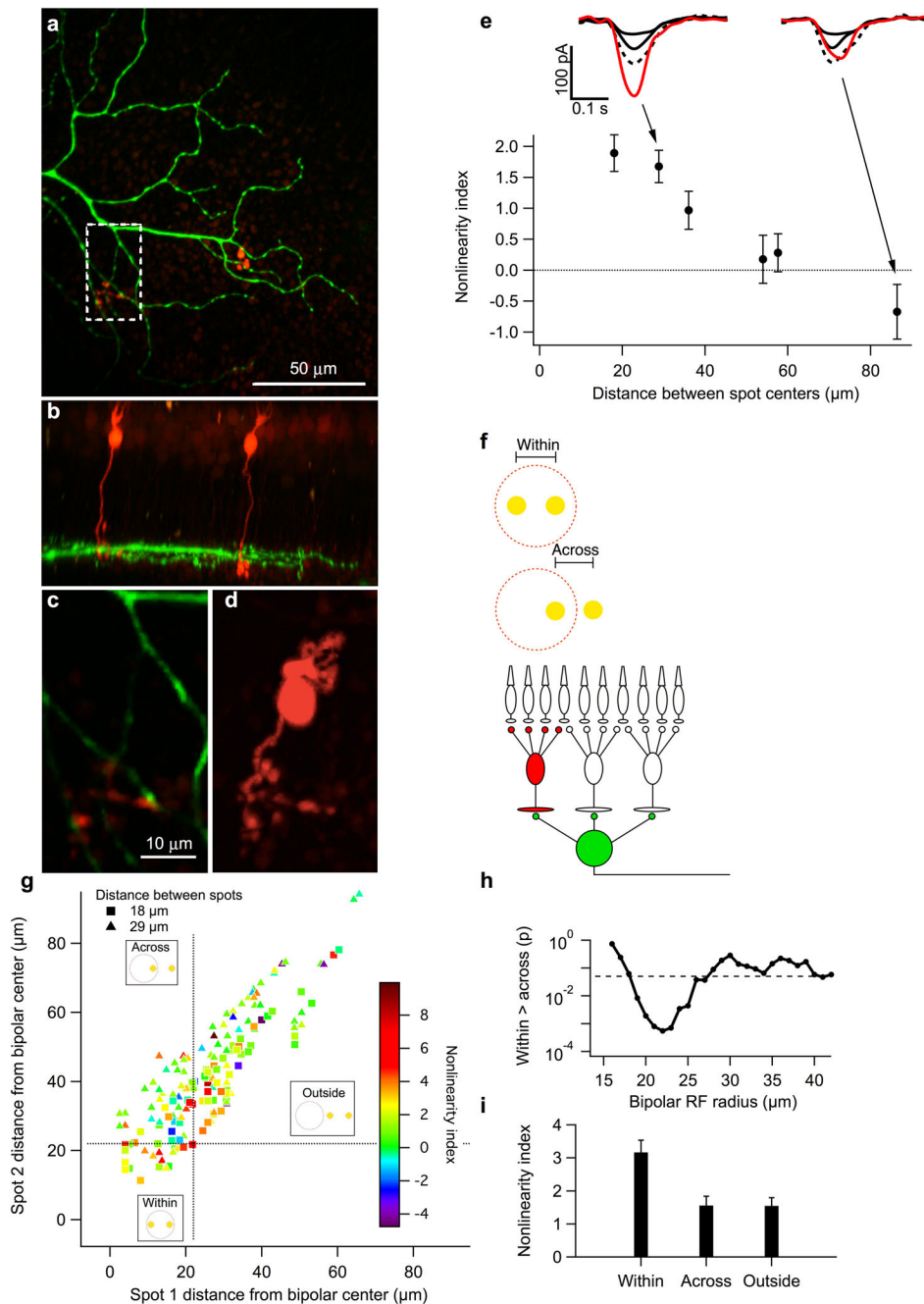
Figure 5. Nonlinear spatial interactions in the receptive field are aligned to the locations of type 6 bipolar cells

a, Maximum intensity projection fluorescence image of the RGC dendrites (green) and genetically labeled bipolar cells (red). **b**, Side view of the RGC and bipolar cells in **a. c**, Magnification of the boxed region in **a** showing the interaction between a type 6 bipolar cell and the RGC dendrites in a 1.5 μm plane of the image stack. **d**, Projection of the type 6 bipolar cell from the axon terminal to the dendrites where the stimuli were aligned (see Methods) in the same region as **c. e**, *top,* Average excitatory input currents to a RGC in

response to small spots presented individually (solid black traces) or simultaneously (red trace). The dashed trace is the linear sum of the individual spot responses. *bottom,* Nonlinearity index (see Methods) as a function of the distance between the centers of the stimulus spots. Error bars are s.e.m. ($n = 291$ total spot pairs in 17 RGCs). **f**, Schematic of the logic of the experiment to determine if type 6 bipolar cells provided nonlinear input to RGCs. We tested the nonlinear interaction between spots that were located either within or across the presumed boundary of a type 6 bipolar cell receptive field. **g**, Nonlinearity index plotted in a color scale for each pair of spots ($n = 170$) with distance between spots either 18 μm or 28 μm. Locations of points along the ordinate and abscissa indicate the distance of each of the two spots from the labelled bipolar cell center (see Methods). Dotted lines indicate the value of the bipolar cell receptive field radius yielding the most significant difference between "within" and "across" regions. **h**, Significance of the statistical test (p value of one-tailed t-test) that the nonlinearity index for "within" bipolar spot pairs exceeds that for "across" bipolar spot pairs plotted as a function of the assumed radius of the bipolar cell receptive field. **i**, Mean nonlinearity index in each region of **g** for a bipolar cell receptive field radius of 22 μm.
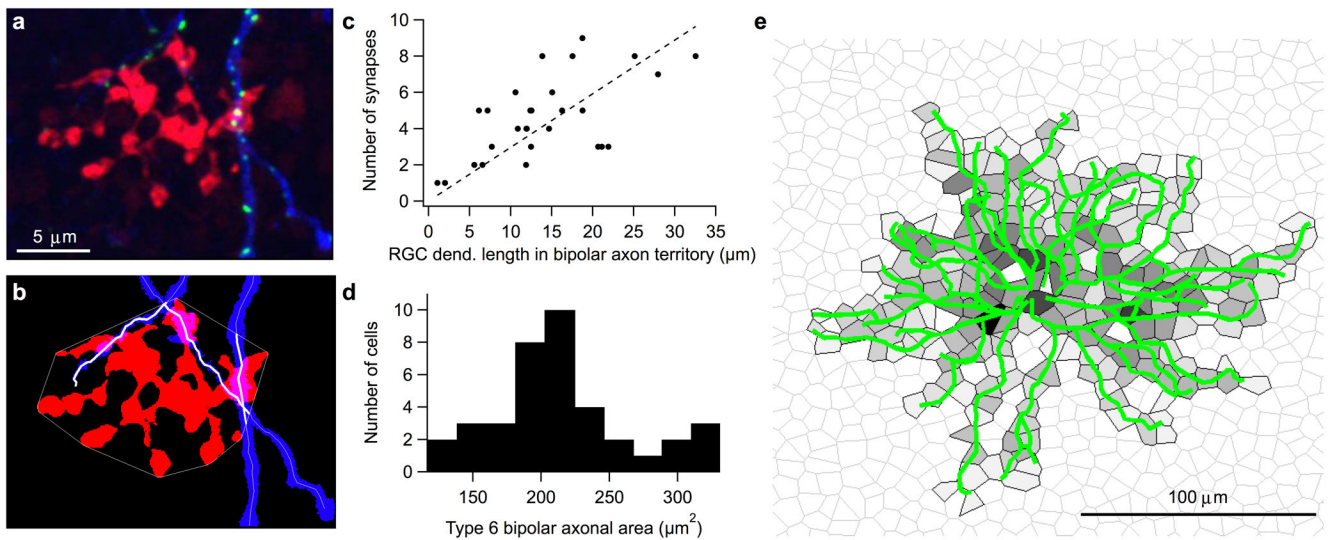
Figure 6. Construction of the bipolar cell weight map from anatomical measurements
a, Image of RGC dendrites (blue), PSD95-YFP (green), and type 6 bipolar cell (red). Putative synapses between the bipolar cell and RGC were counted as in Fig. 3. **b**, RGC dendrites were traced and the length of dendrite in the convex polygonal axonal territory of the bipolar cell axon terminal was measured (thin white lines). **c**, Number of putative synapses as a function of RGC dendritic length in the bipolar cell axon territory ($n = 28$ bipolar cell - RGC pairs; Raw data from ref. 27. Dashed line indicates best fit line through the origin (slope = 0.39 synapses/μm). **d**, Histogram of the bipolar cell axon area (mean = 227 ± 51 μm^2). **e**, Model of bipolar cell weights based on the anatomical measurements in **c** and **d**. Tracing of RGC dendrites (green) and model of bipolar cell synaptic weights. Model bipolar cells with nonzero weights are outlined in black, and darker fill colors correspond to larger weights (see Methods).
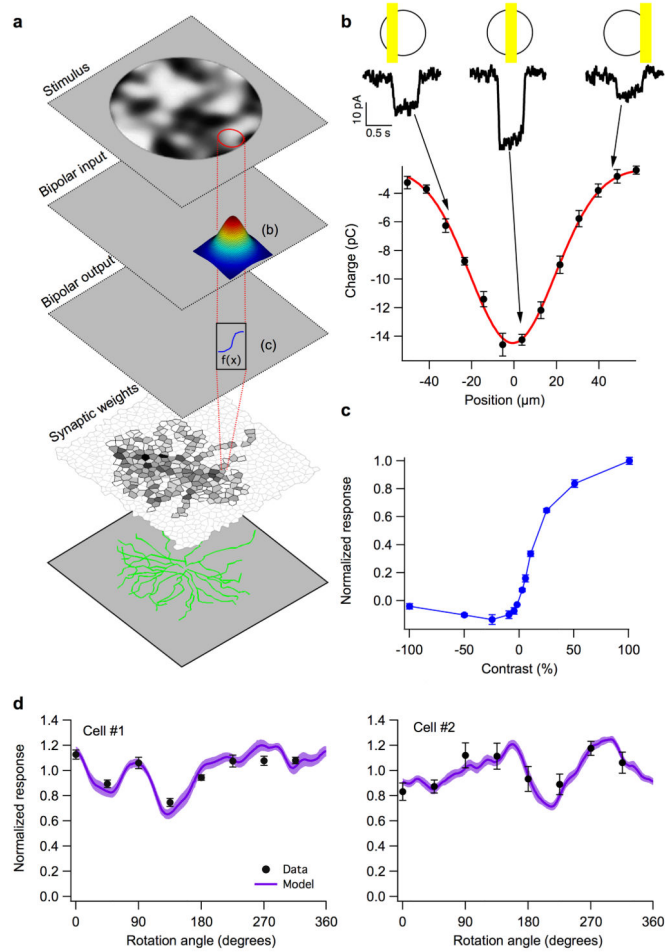
Figure 7. A predictive model of RGC responses to two-dimensional patterns of light

a, Schematic of the model (see Methods for details): 1) The stimulus is sampled by the receptive field of each bipolar cell subunit (see also panel **b**). 2) The resulting input is passed through the nonlinear output function of the bipolar cell (see also panel **c**). 3) The bipolar cell outputs are each weighted by the anatomical model and summed at the RGC. **b**, Measurement of the type 6 bipolar cell receptive field in one dimension. Charge transfer in response to 0.5 s steps of a bright bar (*top*) at different positions were fit by a one-dimensional Gaussian (*bottom*). **c**, Contrast-response function measurement. Uniform 300 μm discs of light were presented to the RGC while measuring excitatory input currents. The charge transfer, normalized to its maximum, is plotted as a function of the contrast of the stimulus. **d**, Response profiles of two RGCs to a texture stimulus at different rotation angles along with model predictions based on the measured nonlinear transfer function and imaged dendrites of each cell. Texture scale was 36 μm. Data points (black) are charge transfer, normalized to the mean, of RGC excitatory input currents (error bars are s.d.). The model prediction was calculated for each degree of rotation. Solid purple line is the mean and shaded region is the s.d. over 10 choices of random seed in the jittering of the bipolar cell grid (see Methods).
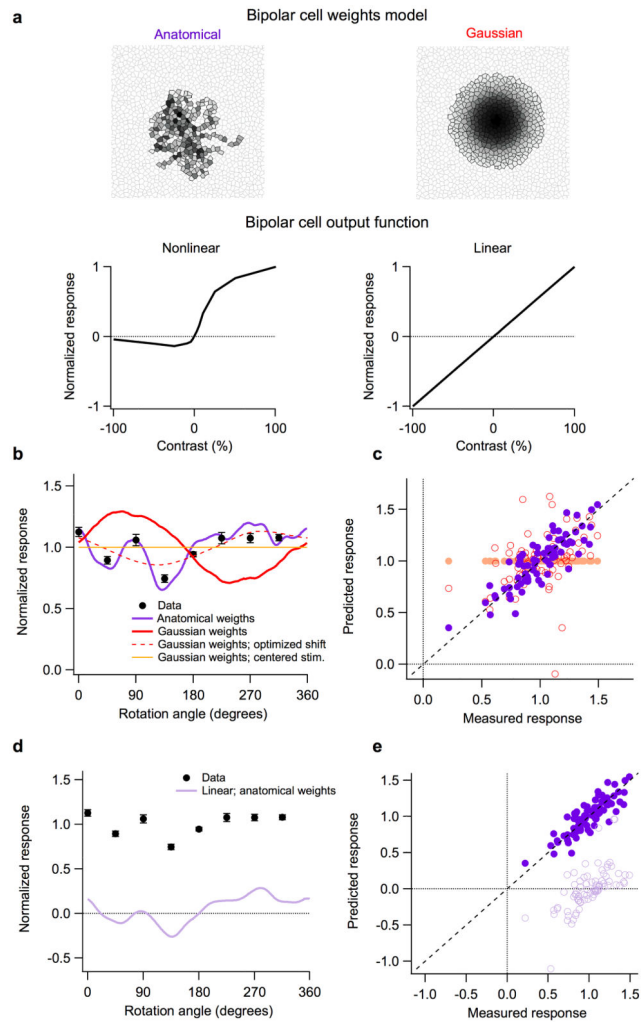
Figure 8. Tests of the predictive power of simplified receptive field models

a, *Top*, Bipolar cell weight maps based on the anatomical model (as in Fig. 6) or a circular two-dimensional Gaussian. Weight maps are normalized so that the darkest colors represent maximal weight, but the sum of the weights was constant across models. *Bottom,* Examples of a measured output nonlinearity, and a linear function replacing the output nonlinearity. **b**, Data from a single cell and predictions from models using the two different bipolar cell weight maps in **a**. The dashed line shows the prediction for an optimized Gaussian model with a free parameter to shift the stimulus relative to the Gaussian weight profile. The orange line shows the prediction for a Gaussian model where the stimulus is perfectly centered (a flat line by construction since the Gaussian weight map was radially symmetric). Error bars on the data are s.d. **c**, Measured responses vs. predictions from the anatomical (purple), Gaussian (red), and centered Gaussian (orange) bipolar weights models for a population of cells. **d**, Data points from **b** along with predictions for a model with linear bipolar cell output and anatomically estimated bipolar cell weights (purple). **e**, Measured responses vs. predictions from the nonlinear (filled symbols) and linear (open symbols) bipolar cell output models for the same population as in **c**. Both models used the

anatomically defined bipolar cell weights. For population data in **c** and **e**, $n = 10$ cells at 80 total rotation angles.